Sustainable Energy & Fuels

ROYAL SOCIETY OF CHEMISTRY

PAPER

View Article Online
View Journal

Cite this: DOI: 10.1039/d6se00152a

Improved reverse water–gas shift chemical looping performance of Co–In-based oxygen carriers supported on ceria

Takuma Higo, * Shuhei Ishizaki, Kenji Ichizuka and Yasushi Sekine *

Indium-based oxygen carriers supported on various oxides were evaluated for the reverse water–gas shift chemical looping (RWGS-CL) at 773 K. Among the materials investigated, 20 wt% $CoIn_2/CeO_2$ showed superior performance, achieving high CO yield and space-time yield, and stable cyclic operation. Comparative studies revealed that, under RWGS-CL conditions, In species supported on CeO_2 exhibited spontaneous dispersion, a behaviour not observed on other oxide supports (γ-Al_2O_3, rutile-TiO_2, anatase-TiO_2, and SiO_2). This dispersion led to the formation of a highly dispersed In surface during operation, which is associated with enhanced CO formation through improved contact with CO_2. Furthermore, Co was found to accelerate the reduction kinetics of In species, likely by promoting H_2 dissociation and hydrogen spillover, while exerting little influence on oxidation kinetics. These results demonstrate that support-dependent structural changes play a key role in determining RWGS-CL performance.

Received 7th February 2026
Accepted 19th April 2026

DOI: 10.1039/d6se00152a

rsc.li/sustainable-energy

1. Introduction

Carbon dioxide (CO_2) emissions associated with anthropogenic activities have raised serious concerns as a major contributor to global warming and related environmental issues.[1,2] Accordingly, the development of carbon capture and utilisation (CCU) technologies has become an urgent priority for the realisation of a decarbonised society.[3] Among the processes for converting captured CO_2 into value-added chemicals, the reverse water–gas shift (RWGS) reaction, shown in eqn (1), is recognised as one of the key reactions.[4,5] Carbon monoxide (CO), the main product of RWGS, is a principal component of synthesis gas and serves as an essential feedstock for a wide range of chemicals.

$$CO_2 + H_2 \leftrightarrow CO + H_2O,\ \Delta_r H^\circ = +42.1\ \text{kJ mol}^{-1} \quad (1)$$

Nevertheless, conventional catalytic RWGS suffers from several inherent limitations, including the requirement for high reaction temperatures, formation of CH_4 as undesired by-product, and the need for costly downstream gas separation. To address these issues at a fundamental level, alternative approaches to the RWGS reaction are required.[4–6]

Reverse water–gas shift chemical looping (RWGS-CL) is regarded as a highly promising extended RWGS process that can fundamentally overcome the intrinsic limitations of conventional catalytic RWGS systems.[7–9] RWGS-CL consists of the following two sequential reaction steps.

$$\text{Reduction step: } MO_x + \delta H_2 \leftrightarrow MO_{x-\delta} + \delta H_2O \quad (2)$$

$$\text{Oxidation step: } MO_{x-\delta} + \delta CO_2 \leftrightarrow MO_x + \delta CO \quad (3)$$

In the reduction step, the metal oxide (MO_x) is reduced by H_2, followed by the oxidation step, in which the reduced metal oxide ($MO_{x-\delta}$) reacts with CO_2 to regenerate MO_x and produce CO. Continuous CO production is achieved through repeated operation of this two-step cycle. The metal oxide that shuttles between these two spatially or temporally separated reactions is referred to as oxygen carrier (OC). By decoupling the reduction and oxidation reactions, RWGS-CL circumvents the thermodynamic limitations of conventional catalytic RWGS, undesired CH_4 formation, and lowers downstream separation costs by simplifying the composition of the outlet gas. In addition to these advantages, the stepwise redox operation in RWGS-CL fundamentally differs from conventional catalytic RWGS, where H_2 and CO_2 coexist in the same reaction environment. In RWGS-CL, the temporal separation of reduction and oxidation steps allows the redox-active species to dynamically change their structure and dispersion state during cycling. Such dynamic changes, which is not typically accessible under steady-state catalytic conditions, can play a crucial role in enabling efficient CO_2 conversion at relatively low temperatures.

Although RWGS-CL offers substantial advantages in principle, significant gaps still remain for it to be realised as an economically viable process. In particular, increasing the product formation rate and shortening the cycle time are priority research challenges for improving the feasibility of

Department of Applied Chemistry, Waseda University, 3-4-1, Okubo, Shinjuku, Tokyo, 169-8555, Japan. E-mail: thigo.catal@gmail.com; ysekine@waseda.jp

chemical looping processes.[10] One effective approach to enhancing productivity is the development of high-performance OCs, particularly in terms of redox capacity and kinetics. As OCs for RWGS-CL, a wide variety of materials have been proposed, including composite oxides based on Fe,[11,12] In,[13,14] and Ga,[15] as well as oxygen-nonstoichiometric oxides such as perovskites[4,16–18] and CeO_2.[19,20] Furthermore, previous studies have demonstrated that supporting these materials on high-surface-area supports can significantly enhance the performance of OCs.[21–30] The introduction of support materials is considered to improve key properties of OCs, including pore volume, surface area, and resistance to sintering, thereby enhancing their productivity. By appropriately combining redox-active species with suitable support materials, there is considerable potential to develop OC materials with more advanced and innovative performance.

In this study, a series of Co–In-based OCs supported on various oxides were prepared and their RWGS-CL performances were systematically compared. Among the OCs screened, 20 wt% $CoIn_2/CeO_2$ exhibited superior performance, its structure and reaction mechanism were investigated in detail. The redox behaviour and reaction kinetics were evaluated using fixed-bed reactor tests, the structural and electronic states of the OCs were investigated by electron microscopy, and *in situ* X-ray absorption fine structure (XAFS) and *in situ* X-ray diffraction (XRD) measurements.

2. Experimental

2.1 Material preparation

In this study, oxygen carriers (OCs) containing 15.9 wt% In and 4.1 wt% Co on a metal-weight basis, corresponding to 1.38 mmol of In and 0.69 mmol of Co per gram of OC ($CoIn_2/CeO_2$), were prepared by impregnation with CeO_2 (JRC-CEO-1, supplied by the Catalysis Society of Japan) as the support. First, CeO_2 and 20 mL of distilled water were placed in a 200 mL round-bottom flask and stirred at 120 rpm under reduced pressure for 30 min using a rotary evaporator. Subsequently, $In(NO_3)_3 \cdot nH_2O$ (Kanto Chemical Co., Inc.) and $Co(NO_3)_2 \cdot 6H_2O$ (Kanto Chemical Co., Inc.), used as metal precursors, were dissolved in distilled water and added to the same flask, followed by additional stirring under reduced-pressure for 20 min. The solvent was then gradually evaporated under reduced pressure using a water bath. After partial removal of water, the slurry was transferred to an evaporating dish and dried to completeness by heating on a hot stirrer. The resulting solid was dried overnight at 393 K in an oven and then calcined in a muffle furnace. Calcination was carried out by heating to 873 K at a ramp rate of 10 K min^{-1} and holding for 5 h.

The prepared OC had a molar ratio of Co to In of 1 : 2, and because the total loading of Co and In corresponded to 20 wt%, it is denoted as 20 wt% $CoIn_2/CeO_2$. Using the same procedure, OCs supported on γ-Al_2O_3 (JRC-ALO-6), SiO_2 (JRC-SIO-11), anatase-type TiO_2 (a-TiO_2, JRC-TIO-7), and rutile-type TiO_2 (r-TiO_2, JRC-TIO-16) were also prepared. All oxide supports used in this study were supplied by the Catalysis Society of Japan.

For performance comparison, a previously reported material (Co–In_2O_3) was prepared by impregnating 16.5 wt% Co onto separately synthesised In_2O_3. The procedure was identical to the impregnation method described above, except that the calcination temperature was 773 K. In_2O_3 was prepared by a citric-acid complex polymerisation method. $In(NO_3)_3 \cdot nH_2O$ was used as the precursor and dissolved in distilled water together with citric acid and ethylene glycol (Kanto Chemical Co., Inc.), each added in a threefold molar ratio relative to indium, in a Teflon beaker. The resulting solution was heated to 573 K and stirred with a hot stirrer to evaporate the solvent to dryness. The obtained solid was then subjected to two-step calcination in a muffle furnace, consisting of pre-calcination at 673 K for 10 h followed by final calcination at 1123 K for 10 h.

2.2 Isothermal RWGS-CL tests

Isothermal RWGS-CL tests were carried out at atmospheric pressure using a fixed-bed flow reactor. The reaction temperature was maintained at 773 K, and the total gas flow rate was set to 100 mL min^{-1}. First, the reactor was heated from room temperature to 773 K at a heating rate of 20 K min^{-1} under an Ar flow. After reaching the target temperature, the reduction step was conducted by flowing 10 vol% H_2 diluted in Ar for 15 min. In the subsequent oxidation step, 10 vol% CO_2 diluted in Ar was supplied until no further CO formation was detected. One sequence consisting of the reduction and oxidation steps was defined as one RWGS-CL cycle. The produced CO was detected and quantified using a quadrupole mass spectrometer (QIC-20, Hiden Analytical). OC particles sieved to a size range of 0.355–0.5 mm were packed into a quartz reactor tube (outer diameter 8 mm, inner diameter 6 mm) with a weight of 0.15 g. The amount of CO produced during the oxidation step was quantified using a calibration curve, and the following evaluation metrics were calculated.

(1) Amount of CO produced (mmol): the integrated amount of CO generated during the oxidation step.

(2) CO yield (mmol g^{-1}): the value in (1) divided by 0.15 and normalised to amount of CO produced per 1 g of OC.

(3) Oxidation completion time (s): defined as the time point at which the instantaneous CO formation rate, calculated from the temporal variation of the mass spectrometric signal and expressed in mmol g^{-1} h^{-1}, decreased below 2 mmol g^{-1} h^{-1}.

(4) Space-time yield of CO (STY, mmol g^{-1} h^{-1}): calculated by dividing (2) by (3), representing the space-time yield of CO generated during the oxidation step.

(5) Overall CO_2 conversion during the complete oxidation cycle: defined as the ratio of the total amount of CO produced to the total amount of CO_2 supplied during the oxidation completion time.

(6) Reduction degree: defined as the ratio of the amount of CO produced to the amount of oxygen available in the oxygen carrier. For Co–In_2O_3, the theoretical amount of oxygen was calculated to be 9.02 mmol g^{-1}. Accordingly, for the oxygen carriers containing 20 wt% $CoIn_2$, the maximum oxygen release from In_2O_3 was estimated to be 2.08 mmol g^{-1}, and this value was used to calculate the reduction degree for γ-Al_2O_3 and SiO_2

supported samples. For TiO_2- and CeO_2-supported samples, the available oxygen amount was experimentally determined by TG–DTA measurements under 10 vol% H_2 at 773 K for up to 120 min, and this value was used for the calculation of the reduction degree.

In the present experimental setup, accurate quantification of H_2O formation during the reduction step was technically challenging. Therefore, the CO yield is also treated as an indicator of the reduction rate. RWGS-CL cycle tests conducted using thermogravimetric analysis confirmed that all OCs investigated in this study are capable of regenerating nearly 100% of the lattice oxygen released during the reduction step in the subsequent oxidation step (in Fig. S1). Accordingly, the amount of CO produced in the flow reactor experiments can be regarded as equivalent to the amount of oxygen reduced during the reduction step. Because the reduction time was fixed when comparing the performance of different OCs, the relative magnitude of the CO yield can be considered to reflect the relative reduction rates of the OCs.

The CO_2 conversion during the oxidation step was measured using the same reactor system. After heating under the same conditions, the OC was reduced in the reduction step using 50 vol% H_2 for 30 min. After the reduction step, the system was purged with Ar. Then, 100 vol% CO_2 was supplied at a prescribed flow rate until oxidation was completed. The sample weight was fixed at 1.00 mg.

The CO_2 conversion was calculated using the following equation:

$$CO_2 \text{ conversion } [\%] = \frac{F_{CO}}{F_{CO_2} + F_{CO}} \times 100$$

where F_{CO} and F_{CO_2} represent the molar flow rates of CO and CO_2 at the reactor outlet, respectively, in units of mol min^{-1}.

2.3 Characterisation

X-ray diffraction (XRD) measurements were performed to evaluate the crystalline structures of the OC samples. Measurements were carried out using a SmartLab III diffractometer (Rigaku Corp.) operated at 40 kV and 40 mA with Cu Kα radiation. Diffraction patterns were collected over a 2θ range of 10°–90° with a scanning rate of 5° min^{-1}.

Specific surface areas were determined by the Brunauer–Emmett–Teller (BET) method using nitrogen adsorption isotherms. Measurements were conducted with a Gemini VII instrument (Micromeritics Instrument Corp.). Prior to measurement, the samples were pretreated at 473 K for 1 h under a N_2 atmosphere.

Transmission electron microscopy (TEM) observations and energy-dispersive X-ray spectroscopy (EDX) mapping were performed using a field-emission transmission electron microscope (HF-2200, Hitachi) and a scanning transmission electron microscope with an energy-dispersive X-ray spectrometer (STEM-EDX, JEM 2100F (UHR); JEOL).

To evaluate the electronic states and coordination environments of metal species during the RWGS-CL reaction, transmission-mode *in situ* XAFS measurements were conducted at the In K-edge and Ce K-edge. Measurements were performed at the BL14B2 beamline of the SPring-8 in Japan (proposal no. 2024B2102, 2024B1974 and 2024B1036). *In situ* XRD measurements were conducted simultaneously. Disc-shaped pellets of OC powder were used as samples. The samples were first heated from room temperature to 773 K under a He atmosphere. Subsequently, 50 vol% H_2 was introduced and flowed for 10 min. The gas was then switched to He, and XAFS and XRD measurements were carried out. This sequence of reduction and measurement was repeated until no further changes were observed in the XANES spectra. Next, 10 vol% CO_2 was introduced under the same conditions and flowed for 1 min. As in the reduction step, the gas was then switched to He and measurements were performed. This sequence was repeated until no further changes were observed in the XANES spectra. In all steps, the total gas flow rate was maintained at 100 mL min^{-1}. For XAFS measurements, transmission-mode XAFS was performed using two ionisation chambers. Quick-scan mode was employed, with a measurement time of 500 s per scan. For XRD measurements, a flat-panel detector was used as a two-dimensional detector. The camera length was set to 481.5 mm, the X-ray energy during XRD measurements was 27.9 keV, and the exposure time was 180 s. The obtained data, expressed in terms of the scattering vector Q, were converted to equivalent diffraction patterns corresponding to Cu Kα radiation using the equation described below, and the converted spectra are presented in this study.

$$2\theta_{Cu} = 2\sin^{-1}\left(\frac{Q\lambda_{Cu}}{4\pi}\right)$$

Here, λ_{Cu} denotes the wavelength of Cu Kα radiation.

3. Results and discussion

3.1 RWGS-CL performance of supported Co–In_2O_3

Isothermal RWGS-CL cycling tests were conducted to compare the performance of OC materials consisting of 20 wt% $CoIn_2$ supported on various oxides with that of unsupported Co–In_2O_3. Fig. 1 and Table S1 summarise the CO production performance during the oxidation step of the OCs. Unsupported Co–In_2O_3 itself exhibited an average CO yield of 2.11 mmol g^{-1} and a space-time yield (STY) of 11.2 mmol g^{-1} h^{-1} over three cycles. The performance of the supported $CoIn_2$ OCs varied significantly depending on the oxide supports. For r-TiO_2, a-TiO_2 and SiO_2, both the CO yield and STY were lower than those of unsupported Co–In_2O_3, while γ-Al_2O_3 showed only a slightly higher STY. Considering that the amount of Co–In species in the supported oxides is one-fifth of that in Co–In_2O_3, normalisation of the performance with respect to the amount of $CoIn_2$ reveals that, as shown in Table S1, these supported OCs exhibited higher CO yield and STY than Co–In_2O_3. This indicates that both the reduction and oxidation rates of the Co–In species were enhanced in these supported OCs. However, the extent of this enhancement was insufficient to compensate for the decreased amount of Co–In species. In contrast, 20 wt% $CoIn_2$/CeO_2 showed markedly enhanced performance, achieving a CO yield of 2.08 mmol g^{-1}, comparable to that of

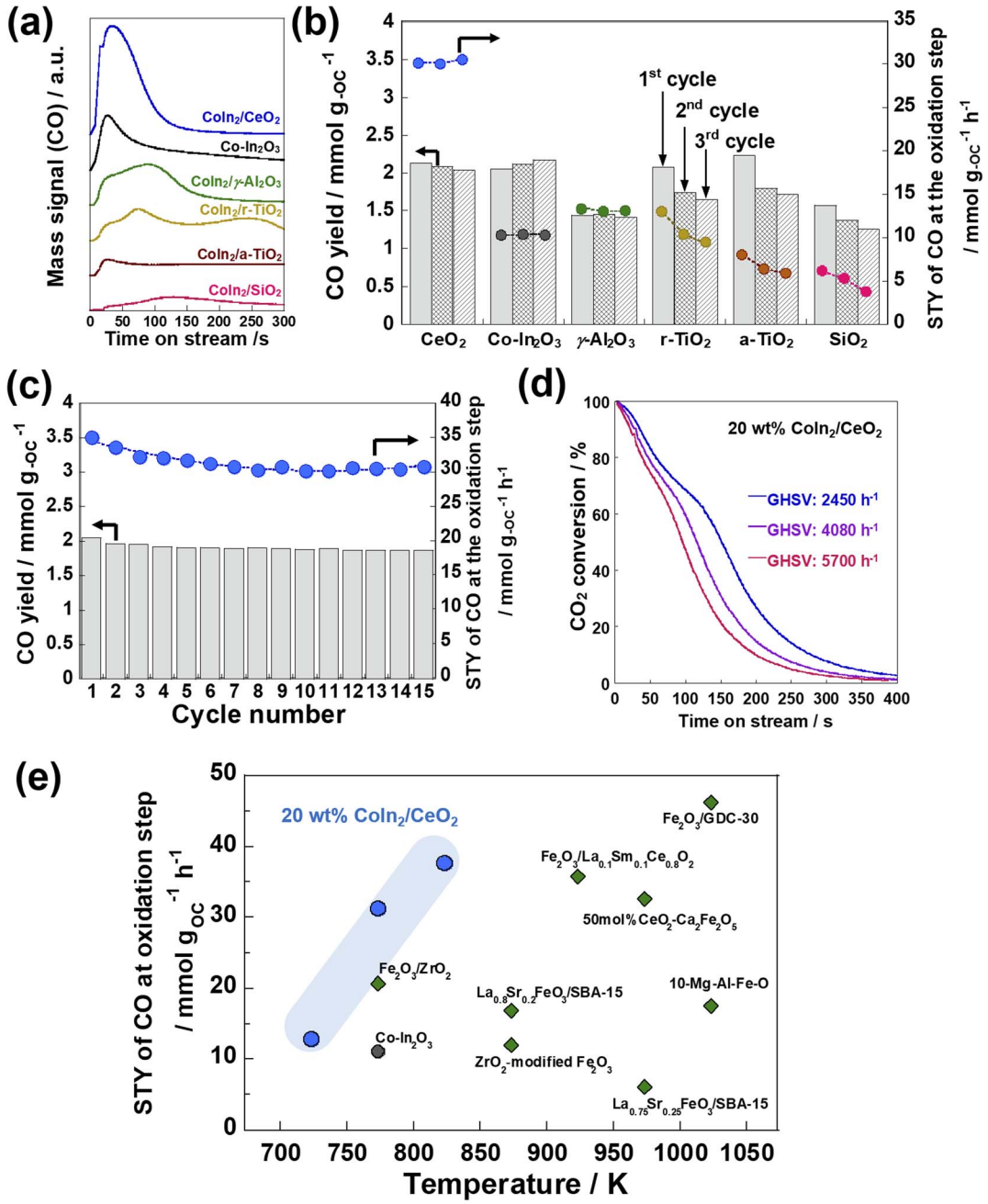

Fig. 1 (a) Mass signal of CO ($m/z = 28$). (b) CO production amount and the space-time yield of CO on the prepared OCs at the oxidation step. (c) Performance of CO production on 20 wt% $CoIn_2/CeO_2$ during the stability test. (d) CO_2 conversion on 20 wt% $CoIn_2/CeO_2$ during the oxidation step using 100 vol% CO_2. (e) Comparison of 20 wt% $CoIn_2/CeO_2$ to other reported supported-type oxygen carriers for RWGS-CL.

Co–In_2O_3, and an STY of 31.2 mmol g^{-1} h^{-1}, which is approximately three times that of Co–In_2O_3. Fig. 1c and Table S3 present the results of a continuous 15-cycle RWGS-CL test conducted to evaluate the performance stability of 20 wt% $CoIn_2/CeO_2$. Although both the CO yield and STY gradually decreased up to the seventh cycle, they subsequently stabilised at approximately 2 mmol g^{-1} and 30 mmol g^{-1} h^{-1}, respectively. In terms of the key functions required for OC materials, namely CO yield, CO space-time yield, and durability, 20 wt% $CoIn_2/CeO_2$ exhibited superior performance. To examine the possible influence of carbon formation under the present reaction conditions, Raman spectra were measured for the $CoIn_2/CeO_2$ before and after RWGS-CL operation. As shown in Fig. S3, no characteristic bands corresponding to carbon species (*i.e.*, D and G bands in the range of 1200–1750 cm^{-1}) were observed, including those after reduction, oxidation, and stability tests. These results indicate that carbon deposition is negligible under the present conditions. Therefore, the CO production behaviour discussed above is not affected by carbon formation.

From the perspective of practical implementation of the RWGS-CL process, OCs that can maintain a high CO_2 conversion during the oxidation step are particularly desirable, as this would reduce the separation and recovery burden associated with unreacted CO_2. Accordingly, the temporal evolution of CO_2 conversion during the oxidation step was evaluated for Co–In_2O_3 and 20 wt% $CoIn_2/CeO_2$. In this evaluation, 1 g of the OC was reduced in 50 vol% H_2 for 60 min, followed by exposure to 100 vol% CO_2 supplied at a prescribed flow rate. Fig. 1d, S4 and Table S4 show the results obtained for Co–In_2O_3 and $CoIn_2/CeO_2$. For unsupported Co–In_2O_3, the CO_2 conversion decreased exponentially from approximately 80% immediately after the start of the oxidation step, and the overall CO_2 conversion in this test was a maximum of 9.5%. In contrast, $CoIn_2/CeO_2$ exhibited an initial CO_2 conversion of approximately 100%, and the conversion behaviour gradually approached a step-function-like, sigmoid profile as the GHSV was decreased. Under these conditions, the overall CO_2 conversion reached a maximum of 20.6%. For achieving high efficiency in the RWGS-CL process, it is ideally desirable that the CO_2 conversion exhibits step-function-type behaviour, allowing a high outlet CO concentration to be maintained while preserving a high space-time yield. As described above, $CoIn_2/CeO_2$ is capable of splitting CO_2 with a very high rate, and therefore is considered capable to maintaining a relatively high conversion rate even under a high-concentration CO_2 feed. Based on this series of performance evaluations, it is evident that CeO_2 is uniquely effective as a support material for Co–In_2O_3.

Fig. 1e and Table S5 compare the performance of 20 wt% $CoIn_2/CeO_2$ with previously reported OCs[14,21–30] for RWGS-CL in terms of reaction temperature and STY. 20 wt% $CoIn_2/CeO_2$ exhibits remarkably high STY values in a relatively low reaction temperature range of 723–823 K, and can therefore be regarded as a highly promising OC material in comparison with previously reported systems.

3.2 Structural characteristics and redox mechanism of Co–In supported CeO_2

Table S6 summarises the BET specific surface areas of the Co–In supported OCs in the as-prepared, after the reduction step, and after the oxidation step. The data for post-reaction were obtained from samples that were cooled to room temperature under an Ar flow after experiencing each step at 773 K, followed by removal from the reactor. All $CoIn_2$-supported OCs exhibited higher specific surface areas than unsupported Co–In_2O_3, both in the as-prepared and after reaction, indicating that an increase in surface area was achieved by supporting. An interesting observation is that $CoIn_2/CeO_2$, which exhibited the highest RWGS-CL performance, possessed the lowest specific surface area among the supported OCs. Therefore, the performance shown in Table S1 cannot be explained by differences in the specific surface area. Fig. 2a shows the EDX mapping

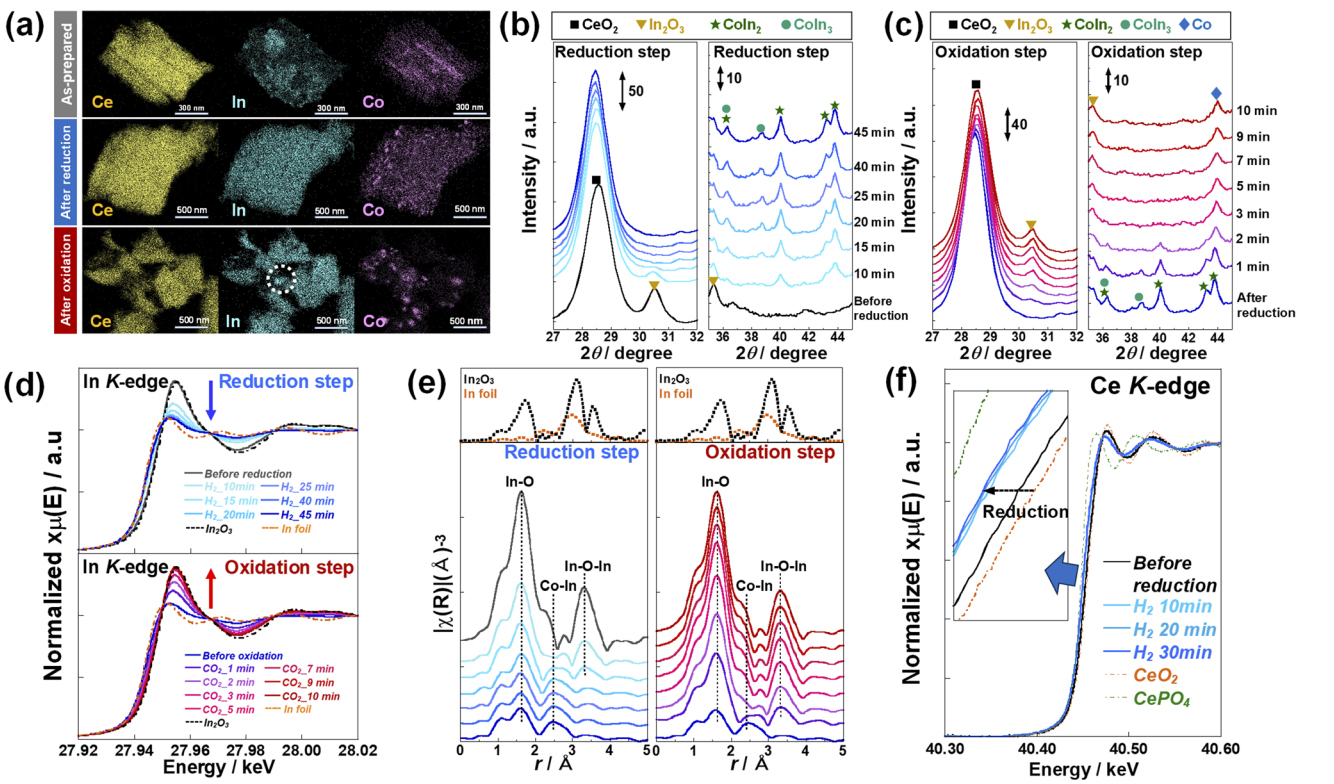

Fig. 2 (a) EDX mapping images of 20 wt% $CoIn_2/CeO_2$ before and after RWGS-CL cycle. *In situ* XRD results of 20 wt% $CoIn_2/CeO_2$ under (b) 50 vol% H_2 (reduction step) and (c) 10 vol% CO_2 (oxidation step) at 773 K. (d) In K-edge XANES spectra of 20 wt% $CoIn_2/CeO_2$ under 50 vol% H_2 (reduction step) and 10 vol% CO_2 (oxidation step) at 773 K. (e) In K-edge EXAFS spectra of 20 wt% $CoIn_2/CeO_2$ under 50 vol% H_2 (reduction step) and 10 vol% CO_2 (oxidation step) at 773 K. (f) Ce K-edge XANES spectra of 20 wt% $CoIn_2/CeO_2$ under 50 vol% H_2 (reduction step) at 773 K.

images of 20 wt% $CoIn_2/CeO_2$ (as-prepared, after reduction and oxidation of 3rd RWGS-CL cycle). In the as-prepared 20 wt% $CoIn_2/CeO_2$, both In and Co were heterogeneously distributed on the CeO_2 support. In contrast, after the reduction step, the mapping images of In and Ce almost completely overlapped, indicating that the In species became uniformly dispersed over the CeO_2 surface. Although some localised regions of Co were still observed, Co was also relatively widely distributed. Following re-oxidation, the overall dispersion of In is largely maintained, although locally aggregated regions can be observed (highlighted by dashed lines). These observations suggest that the dispersion of In species on CeO_2 is significantly improved through the RWGS-CL cycles, while some local heterogeneity remains. The partial aggregation of In after re-oxidation is likely associated with the oxidation of metallic In to In_2O_3, which is also supported by the *in situ* XRD observations discussed later. The localisation of Co became more pronounced. These results indicate that the supported In species on 20 wt% $CoIn_2/CeO_2$ were highly dispersed under RWGS-CL cycling conditions.

To further investigate the redox mechanism of 20 wt% $CoIn_2/CeO_2$, *in situ* XRD and XAFS measurements were performed. Fig. S5 shows the XRD patterns recorded during RWGS-CL cycling at 773 K, while Fig. 2b and c present magnified views of the regions of interest. During the reduction step under a 50 vol% H_2 atmosphere, the intensity of In_2O_3 (ICDD: 00-021-0406) decreased, accompanied by the appearance of diffraction peaks attributable to intermetallic compounds such as $CoIn_2$ (ICDD: 01-091-6508) and $CoIn_3$ (ICDD: 00-041-0880), although their intensities were relatively low. During the subsequent oxidation step under a 10 vol% CO_2 atmosphere, these intermetallic phases disappeared, and In_2O_3 and metallic Co (ICDD: 01-089-4307) were observed. This behaviour indicates that In_2O_3 was reduced by H_2, followed by alloying between metallic In and Co, and that CoIn alloys were subsequently oxidised by CO_2 and separated into metallic Co and In_2O_3. In addition, analysis of the diffraction peak width and intensity provides further insight into the structural evolution during RWGS-CL cycling. The diffraction peak corresponding to $CeO_2(111)$ shows little change in both width and intensity throughout the redox cycles, indicating that the CeO_2 support maintains its structure under the present reaction conditions. In contrast, the diffraction peaks attributed to In_2O_3 after the oxidation step become broader and less intense compared to those of the as-prepared sample. This change suggests a decrease in crystallite size and an increase in the dispersion of In_2O_3 species upon RWGS-CL cycling. It should be noted that no distinct amorphous fraction was observed in the XRD patterns of $CoIn_2/CeO_2$. This indicates that the material remains predominantly crystalline under the present conditions.

The XRD patterns of the other supported OCs exhibited broadly similar behaviour (Fig. S6). In the as-prepared, diffraction peaks corresponding to the support oxides and In_2O_3 were observed. After the reduction step, the In_2O_3 decreased or disappeared, accompanied by the appearance of $CoIn_2$. Following the oxidation step, the $CoIn_2$ phase disappeared, while intense diffraction peaks of In_2O_3 and metallic Co appeared. These results suggest that the redox of In species accompanied by the formation and decomposition of CoIn alloys occurred for all OCs. This behaviour is consistent with the redox mechanism of Co–In_2O_3 reported in our previous study.[14] In contrast, analysis of the diffraction peak width and intensity indicates that a different structural evolution occurs compared to $CoIn_2/CeO_2$. For all samples, the diffraction peaks attributed to In_2O_3 after the oxidation step become significantly more intense and sharper compared to those of the as-prepared state. This indicates an increase in crystallite growth of In_2O_3 during RWGS-CL cycling on these supports, suggesting that In species tend to aggregate and form larger crystalline domains.

Notably, the diffraction intensities of the intermetallic compounds observed for 20 wt% $CoIn_2/CeO_2$ were relatively small compared with those for other OCs with the same loading of Co and In, suggesting that these phases existed on the support in a highly dispersed state. In addition, as shown in Fig. 2a, Co exhibited a localisation greater than In after the reduction step, implying that some In species may not be alloyed with Co. Focusing on the $CeO_2(111)$ diffraction peak, a shift towards lower angles during the reduction and towards higher angles during the oxidation was observed. This behaviour reflects changes in the lattice volume associated with the release and regeneration of lattice oxygen in CeO_2, suggesting that the CeO_2 support itself also undergoes redox during RWGS-CL cycle.

The *in situ* XAFS results shown in Fig. 2d–f are in good agreement with the *in situ* XRD observations. Fig. 2d shows the temporal evolution of the In K-edge XANES spectra during the reduction and oxidation steps. The spectrum before reduction closely matched that of the reference In_2O_3 sample, indicating that In was initially in the In^{3+} state. Under an H_2 atmosphere, the white-line intensity gradually decreased with time, and the spectral shape evolved towards that of In foil, indicating the reduction of In_2O_3 to metallic In species. The XANES spectrum after reduction did not share an isosbestic point with the reference samples (Fig. S7), and therefore linear combination fitting was not applied, most likely due to the contribution of CoIn alloy species formed during reduction. Upon switching to a CO_2 atmosphere, the XANES spectra rapidly returned to a state comparable to that before reduction, indicating reoxidation of the In species by CO_2. In the EXAFS spectra, a peak emerged at approximately 2.5 Å as the reduction progressed. Since this peak did not correspond to In–In scattering, it is attributed to CoIn alloy formation. The Ce K-edge XANES spectra shown in Fig. 2f indicate a slight reduction of Ce^{4+} under the reduction step, which is also consistent with the *in situ* XRD results.

3.3 Evaluation of the roles of individual components in $CoIn_2/CeO_2$

To clarify the roles of the individual components, namely Co, In, and CeO_2, in the high RWGS-CL performance of $CoIn_2/CeO_2$, a series of comparative studies was conducted. Fig. S8, S9 and Tables 1 and S7 summarise the RWGS-CL performance of 15.9 wt% In/CeO_2, 4.1 wt% Co/CeO_2, and bare CeO_2, together

Table 1 Performance for the prepared OCs (20 wt% $CoIn_2/CeO_2$, 15.9 wt% In/CeO_2, 4.1 wt% Co/CeO_2 and CeO_2)

Oxygen carrier	CO production/mmol	CO yield/mmol g^{-1}	Reduction degree/%	Oxidation completion time/s	Space-time yield/mmol g^{-1} h^{-1}	Overall CO_2 conversion/%
20 wt% $CoIn_2/CeO_2$	0.313	2.08	83.3	240	31.2	17.5
15.9 wt% In/CeO_2	0.219	1.46	73.1	146	36.0	20.2
4.1 wt% Co/CeO_2	0.011	0.07	—	77	3.5	1.9
CeO_2	0.011	0.07	—	65	4.0	2.3

with that of 20 wt% $CoIn_2/CeO_2$. The loadings of In and Co were adjusted to match those in 20 wt% $CoIn_2/CeO_2$.

Focusing first on the bare CeO_2, the CO yield was only 0.07 mmol g^{-1}, indicating a very limited contribution. Although CeO_2 itself undergoes redox, its direct contribution to CO formation is considered to be minor. In contrast, 15.9 wt% In/CeO_2 exhibited a CO production of 1.46 mmol g^{-1} and a remarkably high STY of 36.0 mmol g^{-1} h^{-1}, clearly indicating that In species act as the primary redox-active species and the active sites for CO_2 splitting. STEM-EDX images of reduced 15.9 wt% In/CeO_2 (Fig. S10) show that, similar to 20 wt% $CoIn_2/CeO_2$, the In species on CeO_2 are highly dispersed. Fig. 3 compares the XRD patterns of $CoIn_2/Al_2O_3$ and $CoIn_2/CeO_2$ after multiple RWGS-CL cycles. For $CoIn_2/Al_2O_3$, the crystallite size of In_2O_3 increased with increasing cycle number, indicating that aggregation of In and Co species easily progresses on the Al_2O_3 surface. Comparison of the EDX mapping images of $CoIn_2/Al_2O_3$ shown in Fig. S11 with those of $CoIn_2/CeO_2$ in Fig. 2a clearly reveals aggregation of the In species. In contrast, for $CoIn_2/CeO_2$, the crystallite size of In_2O_3 decreased with increasing cycle number. ICP results (Table S8) show that the amount of supported In remained nearly unchanged even after multiple cycles. Therefore, the decrease in In_2O_3 crystallite size cannot be attributed to the loss of In species through volatilisation, but rather indicates dispersion of In species on CeO_2 surface during RWGS-CL cycle. To further clarify the evolution of the dispersion state during RWGS-CL cycling, additional EDX mapping images after 1 cycle and after 15 cycles have been provided in Fig. S12 and S13. Comparison of these results with the 3-cycle data shown in Fig. 2a indicates that In species become significantly dispersed already during the first cycle. Although slight local aggregation of In species is observed after the oxidation step, the overall dispersion is largely maintained throughout the cycling. This suggests that such aggregation is partially reversed during the subsequent reduction step through oxygen release, leading to dispersion of In species on CeO_2 and suppressing excessive aggregation. Furthermore, the dispersion of In species tends to improve with increasing cycle number. This behaviour is consistent with the XRD analysis shown in Fig. 3, where the gradual decrease in crystallite size suggests progressive dispersion of In species during RWGS-CL operation. These results demonstrate that CeO_2 plays a crucial role in inducing spontaneous high dispersion of In species and suppressing their aggregation under reaction conditions through strong metal–support interactions. To further elucidate the origin of this support-dependent dispersion behaviour, XPS analysis was conducted for $CoIn_2/CeO_2$ and $CoIn_2/Al_2O_3$ before and after RWGS-CL cycling. These results are shown in Fig. S14. For $CoIn_2/CeO_2$, the In 3d peak exhibited a shift of approximately 0.5 eV toward higher binding energy after cycling, whereas no noticeable shift was observed for $CoIn_2/Al_2O_3$. This result indicates that the electronic state of In species is modified specifically on the CeO_2 support, suggesting a interaction between In species and CeO_2.[31] Considering the redox properties of CeO_2 and its ability to form oxygen vacancies, such

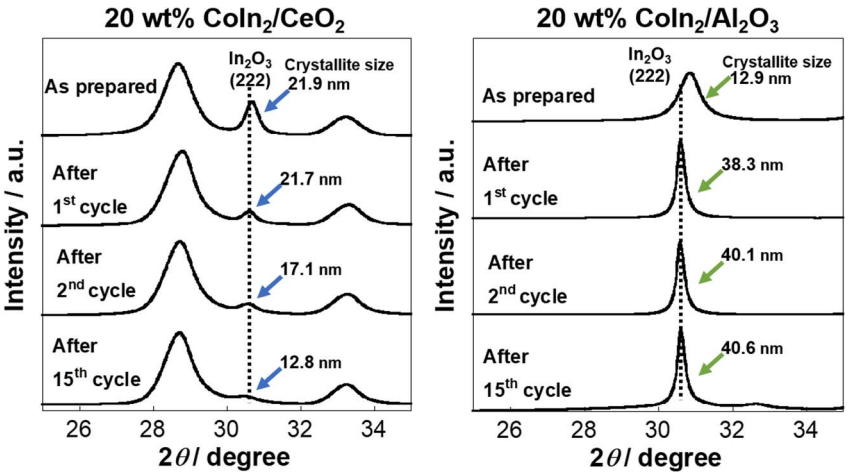

Fig. 3 Crystallite size of In_2O_3 on XRD patterns for $CoIn_2/CeO_2$ and $CoIn_2/Al_2O_3$.

interaction may contribute to the spontaneous dispersion of In species under RWGS-CL conditions.

Next, the role of Co was examined. As evidenced by *in situ* XRD, metallic Co was observed even after the oxidation step, indicating that Co undergoes little redox under RWGS-CL conditions at 773 K. Accordingly, the CO yield on 4.1 wt% Co/CeO_2 was nearly identical to that on bare CeO_2. However, the CO yield on 20 wt% $CoIn_2/CeO_2$ was approximately 1.4 times higher than that of 15.9 wt% In/CeO_2. Since the amount of CO produced during the oxidation step corresponds to the amount of In reduced during the preceding reduction step, Co is considered to enhance the reduction rate of supported In species. Fig. 4a and Tables S9, S10 compare the RWGS-CL performance of OCs with varying Co to In ratios. Regardless of the amount of supported Co, the CO yield was consistently approximately 2 mmol g^{-1}, indicating that even a small amount of Co provides a comparable enhancement effect. To clarify whether Co contributes to the dispersion of In species, additional STEM-EDX mapping images of In/CeO_2 (without Co) before and after oxidation are provided in Fig. S15. In the as-prepared sample, In species exhibit a clearly inhomogeneous distribution, whereas after oxidation, they become relatively well dispersed on the CeO_2 support. Combined with the EDX results after the reduction step shown in Fig. S11, these observations indicate that the dispersion of In species occurs on CeO_2 even in the absence of Co. Therefore, Co does not contribute to the dispersion of In species.

To further elucidate the role of Co, kinetic analyses based on the Hancock–Sharp method[32–34] were performed. The experimental data used for fitting the reaction models were obtained by thermogravimetric analysis. The weight loss observed under a 10 vol% H_2 flow was assumed to correspond to oxygen released from the OCs, and the reduction degree of each OC was calculated accordingly. Fig. S16 shows the fitting results of the model reaction rate equations to the experimental data. For all OC materials, the Avrami–Erofe'ev nucleation-and-growth model[35–37] provided the best fit to the experimental data for all OC materials. Arrhenius plots constructed using the obtained rate constants k_{red} are shown in Fig. 4b. The apparent activation energy of In/CeO_2 without Co (Co/In = 0) was 81.8 kJ mol^{-1}, whereas $CoIn_8/CeO_2$ (Co/In = 0.125) and $CoIn_2/CeO_2$ (Co/In = 0.5) exhibited values approximately 21–29 kJ mol^{-1} lower. This enhancement in the reducibility of In species is attributed to promoted H_2 dissociation on metallic Co particles and subsequent H spillover to surface In species. The promotion of In_2O_3 reduction *via* H spillover mediated by metal nanoparticles such as noble metals,[38] Ni,[39] and Co[40] has been widely reported. The series of $CoIn_x/CeO_2$ investigated here possessed sufficient Co loading and surface distribution to supply dissociated hydrogen to surface In species at a sufficiently high rate, resulting in a Co-loading-independent enhancement effect.

Kinetic analysis of the oxidation step was also conducted using the Hancock–Sharp method (Fig. 4c and S17). As expected, the rate constants k_{ox} were nearly identical regardless of the presence or absence of Co. Therefore, Co in $CoIn_2/CeO_2$

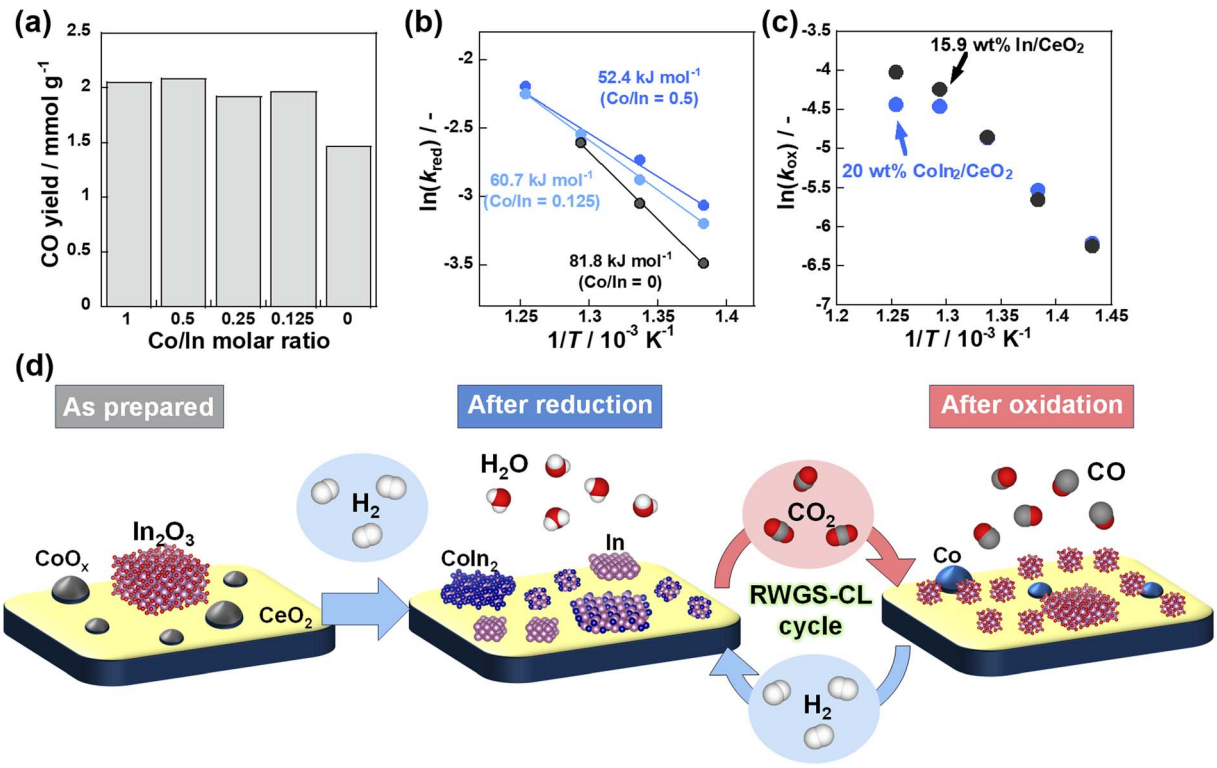

Fig. 4 (a) CO yield of $CoIn_x/CeO_2$ with different Co/In ratios. (b) Arrhenius plots and apparent activation energies for the reduction step. (c) Arrhenius plots for the oxidation step. (d) Schematic illustration of the structural features and redox mechanism of $CoIn_2/CeO_2$.

primarily contributes to enhancing the reaction rate of the reduction step, whereas the high CO formation rate during the oxidation step is mainly attributed to the dramatically increased contact frequency between CO_2 and highly dispersed In species.

Fig. 4d schematically illustrates the structural features and reaction mechanism of Co–In supported CeO_2 OC materials, including 20 wt% $CoIn_2/CeO_2$. In the as-prepared state, Co and In are present as oxide species that are sparsely and heterogeneously distributed on the CeO_2 surface. Upon exposure to an H_2 atmosphere during the reduction step, both Co and In are reduced to their metallic states, accompanied by the formation of Co–In alloys such as $CoIn_2$. Metallic Co functions as an active site for H_2 dissociation, thereby promoting the reduction of In species *via* hydrogen spillover. Simultaneously, dispersion of In species occurs, leading to the formation of CeO_2 surface uniformly covered with In species. During the subsequent oxidation step, the metallic In species and Co–In alloys react with CO_2 to produce CO, while In is selectively reoxidised to In_2O_3. Notably, the In species remain highly dispersed without excessive aggregation, leading to a surface structure in which sparsely distributed metallic Co nanoparticles coexist with uniformly dispersed In_2O_3. Thereafter, RWGS-CL cycling proceeds through the redox of highly dispersed In species on the CeO_2. The high dispersion of In species is considered to increase the contact frequency with CO_2, resulting in an enhanced CO formation rate. An additional advantage of Co–In supported CeO_2 is that such spontaneous dispersion is induced under RWGS-CL reaction conditions, enabling preparation by a simple impregnation method without the need for elaborate structural design of the support material. This effective utilisation of metal–support interactions represents a promising strategy for the rational design of advanced OC materials.

4. Conclusion

In this study, the performance of indium-based oxygen carriers supported on various oxides was systematically investigated for the RWGS-CL process. Among the OCs examined, $CoIn_2/CeO_2$ exhibited simultaneously high CO yield and space-time yield, and stable performance. A notable experimental observation was that In species supported on CeO_2 underwent spontaneous dispersion under reaction conditions, whereas such behaviour was not observed on the other oxide supports examined. This dispersion behaviour resulted in a highly dispersed In surface during RWGS-CL operation, which is considered to contribute to the enhanced CO formation rate through increased contact frequency with CO_2. In addition, the presence of Co was found to promote the reduction kinetics of the supported In species, likely *via* enhanced H_2 dissociation and hydrogen spillover, while having a negligible influence on the oxidation kinetics. This result demonstrates that the choice of support can critically influence the structural evolution of oxygen carriers under RWGS-CL cycle. These findings highlight the importance of considering support-induced dispersion behaviour in the design of RWGS-CL oxygen carriers and suggest that high-performance OCs can be realised by exploiting such effects using simple preparation methods such as impregnation.

Author contributions

Conceptualisation: TH and YS, funding acquisition: YS, investigation: TH, SI and KI, project administration: YS, supervision: YS, validation: TH, SI, KI and YS, visualization: TH, writing – original draft: TH, writing – review and editing: YS.

Conflicts of interest

There are no conflicts to declare.

Data availability

The data supporting this article have been included as part of the supplementary information (SI). Supplementary information is available. See DOI: https://doi.org/10.1039/d6se00152a.

Acknowledgements

We appreciate Dr Takeshi Watanabe (Japan Synchrotron Radiation Research Institute, SPring-8) for his great support with *in situ* XAFS and XRD measurements in BL14B2. Equipment (JEM-2100F: Material Characterization Central Laboratory in Waseda University) shared with the MEXT Project for Promoting Public Utilization of Advanced Research Infrastructure (program for supporting the construction of core facilities) under grant number JPMXS0440500023 was used. A part of this work was supported by JST-ALCA-Next Program Grant Number 23836167, Japan, by JSPS KAKENHI 24H00487, 23H05404, 23K20034, Japan.

References

1 Intergovernmental Panel on Climate Change (IPCC), *Climate Change 2021: The Physical Science Basis, Contribution of Working Group I to the Sixth Assessment Report of the Intergovernmental Panel on Climate Change*, Cambridge University Press, 2023, pp. 35–144.
2 S. J. Davis, K. Caldeira and H. D. Matthews, *Science*, 2010, **329**, 1330–1333.
3 B. Dziejarski, R. Krzyżyńska and K. Andersson, *Fuel*, 2023, **342**, 127776.
4 Y. A. Daza and J. N. Kuhn, *RSC Adv.*, 2016, **6**, 49675–49691.
5 M. L. T. Triviño, N. C. Arriola, Y. S. Kang and J. G. Seo, *Chem. Eng. J.*, 2024, **487**, 150369.
6 W. Zhang, J. Sun, H. Wang and X. Cui, *Chem.–Asian J.*, 2024, **19**, e202300971.
7 Y. A. Daza, R. A. Kent, M. M. Yung and J. N. Kuhn, *Ind. Eng. Chem. Res.*, 2014, **53**(14), 5828–5837.
8 M. Wenzel, L. Rihko-Struckmann and K. Sundmacher, *AIChE J.*, 2017, **63**(1), 15–22.
9 K. Kang, H. Sampei and Y. Sekine, *RSC Sustainability*, 2025, **3**, 1598–1628.
10 J.-P. Lange, V. L. Sushkevich, A. J. Knorpp and J. A. van Bokhoven, *Ind. Eng. Chem. Res.*, 2019, **58**, 8674–8680.
11 Y. Qiu, L. Ma, D. Zeng, M. Li, D. Cui, Y. Lv, S. Zhang and R. Xiao, *J. Energy Chem.*, 2020, **46**, 123–132.

12 L. Ma, Y. Qiu, M. Li, D. Cui, S. Zhang, D. Zeng and R. Xiao, *Ind. Eng. Chem. Res.*, 2020, **59**, 6924–6930.
13 J. Makiura, T. Higo, Y. Kurosawa, K. Murakami, S. Ogo, H. Tsuneki, Y. Hashimoto, Y. Sato and Y. Sekine, *Chem. Sci.*, 2021, **12**, 2108–2113.
14 J. Makiura, S. Kakihara, T. Higo, N. Ito, Y. Hirano and Y. Sekine, *Chem. Commun.*, 2022, **58**, 4837–4840.
15 K. Kang, S. Kakihara, T. Higo, H. Sampei, K. Saegusa and Y. Sekine, *Chem. Commun.*, 2023, **59**, 11061–11064.
16 H. Z. Shi, V. R. Bhethanabotla and J. N. Kuhn, *J. CO_2 Util.*, 2021, **51**, 101638.
17 A. E. Ramos, D. Maiti, Y. A. Daza, J. N. Kuhn and V. R. Bhethanabotla, *Catal. Today*, 2019, **338**, 52–59.
18 Y. Goto, K. Yamazaki, M. Kikugawa and M. Aoki, *Dalton Trans.*, 2024, **53**, 13847–13853.
19 T. Higo, K. Saegusa, S. Ishizaki, S. Kakihara, Y. Yayama, Y. Hirano and Y. Sekine, *J. Phys. Chem. C*, 2025, **129**(44), 19786–19793.
20 F. J. Pomiro, G. G. Fouga, A. E. Tamietti, A. E. Bohé and G. D. Micco, *Chem. Eng. J.*, 2024, **498**, 155222.
21 E. Sun, G. Wan, V. Haribal, J. Rojas, R. Gupta and A. Majumdar, *Cell Rep. Phys. Sci.*, 2025, **4**(9), 101581.
22 A. Jo, Y. Kim, H. S. Lim, M. Lee, D. Kang and J. W. Lee, *J. CO_2 Util.*, 2022, **56**, 101845.
23 B. J. Hare, D. Maiti, Y. A. Daza, V. R. Bhethanabotla and J. N. Kuhn, *ACS Catal.*, 2018, **8**(4), 3021–3029.
24 B. Jin, H. Poelman, C. Detavernier, Z. Liang, G. B. Marin and V. V. Galvita, *Appl. Catal., B*, 2021, **292**, 120194–120204.
25 J. Zhao, Y. W. Xiong, Z. H. Gao, F. Y. Fu, L. L. Niu and M. Jin, *Sustainable Energy Fuels*, 2022, **6**(5), 1448–1457.
26 J. C. Brower, B. J. Hare, V. R. Bhethanabotla and J. N. Kuhn, *ChemCatChem*, 2020, **12**(24), 6317–6328.
27 Z. Sun, K. Lei, L. R. Smith, N. F. Dummer, R. J. Lewis, H. Qi, K. J. Aggett, S. H. Taylor, Z. Sun and G. J. Hutchings, *Carbon Energy*, 2025, **7**(9), e70011.
28 D. Zeng, Y. Qiu, L. Ma, M. Li, D. Cui, S. Zhang and R. Xiao, *Environ. Sci. Technol.*, 2020, **54**(19), 12467–12475.
29 N. V. R. A. Dharanipragada, L. C. Buelens, H. Poelman, E. D. Grave, V. V. Galvita and G. B. Marin, *J. Mater. Chem. A*, 2015, **3**, 16251.
30 L. C. Buelens, A. Dharanipragada, H. Poelman, Z. Zhou, G. B. Marin and V. V. Galvita, *J. CO_2 Util.*, 2019, **29**, 36.
31 X. Liu, K. Wang, D. Cao, C. Li, L. Wang, M. Wang, Q. Li, C. Wu and K. Liu, *Fuel*, 2024, **362**, 30760.
32 J. D. Hancock and J. H. Sharp, *J. Am. Ceram. Soc.*, 1972, **55**, 74–77.
33 K. Piotrowski, K. Mondal, H. Lorethova, L. Stonawski, T. Szymański and T. Wiltowski, *Int. J. Hydrogen Energy*, 2005, **30**, 1543–1554.
34 Z. Zhou, L. Han and G. M. Bollas, *Int. J. Hydrogen Energy*, 2014, **39**, 8535–8556.
35 M. Avrami, *J. Chem. Phys.*, 1939, **7**, 1103–1112.
36 M. Avrami, *J. Chem. Phys.*, 1940, **8**, 212–224.
37 M. Avrami, *J. Chem. Phys.*, 1941, **9**, 177–184.
38 N. Rui, Z. Wang, K. Sun, J. Ye, Q. Ge and C.-J. Liu, *Appl. Catal., B*, 2017, **218**, 488–497.
39 Y. Cai, C. Lin, X. Cha, Y. Wu, X. Rao, K. B. Tan, D. Cai, G.-L. Zhuang and G. Zhan, *ACS Catal.*, 2024, **14**(11), 8463–8479.
40 M. Zhang, H. Chen, K. Cheng, L. Zhao, H. Huang, J. Kang, Q. Zhang and Y. Wang, *J. Phys. Chem. C*, 2025, **129**(5), 2535–2545.

